

The DR21(OH) trident — resolving the massive ridge into three entangled fibers as the initial condition of cluster formation

YUE CAO,^{1,2,3} KEPING QIU,^{1,2} QIZHOU ZHANG,³ AND GUANG-XING LI⁴

¹*School of Astronomy and Space Science, Nanjing University, 163 Xianlin Avenue, Nanjing 210023, People's Republic of China*

²*Key Laboratory of Modern Astronomy and Astrophysics (Nanjing University), Ministry of Education, Nanjing 210023, People's Republic of China*

³*Center for Astrophysics | Harvard & Smithsonian, 60 Garden Street, MS 42, Cambridge, MA 02138, USA*

⁴*South-Western Institute for Astronomy Research, Yunnan University, Kunming, 650500 Yunnan, People's Republic of China*

Submitted to ApJ

ABSTRACT

DR21(OH) ridge, the central part of a high-mass star and cluster forming hub-filament system, is resolved spatially and kinematically into three nearly parallel fibers (f1, f2, and f3) with a roughly north-south orientation, using the observations of molecular transitions of H¹³CO⁺ (1 – 0), N₂H⁺ (1 – 0), and NH₂D (1_{1,1} – 1_{0,1}) with the Combined Array for Research in Millimeter Astronomy. These fibers are all mildly supersonic (σ_v about 2 times the sound speed), having lengths around 2 pc and widths about 0.1 pc, and they entangle and conjoin in the south where the most active high-mass star formation takes place. They all have line masses 1–2 orders of magnitude higher than their low-mass counterparts and are gravitationally unstable both radially and axially. However, only f1 exhibits high-mass star formation all the way along the fiber, yet f2 and f3 show no signs of significant star formation in their northern parts. A large velocity gradient increasing from north to south is seen in f3, and can be well reproduced with a model of free-fall motion toward the most massive and active dense core in the region, which corroborates the global collapse of the ridge and suggests that the disruptive effects of the tidal forces may explain the inefficiency of star formation in f2 and f3. On larger scales, some of the lower-density, peripheral filaments are likely to be the outer extensions of the fibers, and provide hints on the origin of the ridge.

Keywords: Interstellar filaments (842); Dense interstellar clouds (371); Star formation (1569); Star forming regions (1565); Young massive clusters (2049); Dust continuum emission (412); Interstellar line emission (844)

1. INTRODUCTION

Filamentary structures have been widely known to pervade the cold interstellar medium (e.g., [André et al. 2010, 2014](#); [Molinari et al. 2010](#); [Schisano et al. 2014](#)). While molecular filaments span a wide range in length and density, over the past decade dense filaments of clump to cloud scales, i.e., 1–10 pc, are extensively studied as they may bridge relatively diffuse molecular gas and compact cores capable of forming individual stars or multiple stars. Although it is not impossible to find filaments in relative isolation (e.g., [Hacar et al. 2016](#)), more often they appear to be organized into more complex structures, such as a web-like network or nest (e.g., [Men'shchikov et al. 2010](#); [Arzoumanian et al. 2011](#); [Hill et al. 2011](#); [Busquet et al. 2013](#)), or a system of several filaments converging at a high-density region, i.e., a hub-filament system (HFS, e.g., [Galván-Madrid et al. 2010](#); [Liu et al. 2012](#); [Schneider et al. 2012](#); [Kirk et al. 2013](#); [Peretto et al. 2014](#); [Williams et al. 2018](#)). Massive and elongated hub regions are sometimes referred to as “ridges” (e.g., [Hill et al. 2011](#); [Hennemann et al. 2012](#); [Tigé et al. 2017](#); [Motte et al. 2018](#)). HFSs are of particular interests to the formation of massive stars and clusters since the hubs or ridges are located close to the gravity center and thus may aid in global collapse or large-scale gas inflow along the filaments ([Myers 2009](#); [André et al. 2014](#); [Kumar et al. 2020](#)). And observed velocity fields in some massive filaments and HFSs are consistent with global collapse at a high accretion

rate of order $10^{-3} M_{\odot} \text{ yr}^{-1}$ (e.g., Schneider et al. 2010; Zernickel et al. 2013; Hu et al. 2021), pointing to a dynamic picture of cluster formation (Krumholz et al. 2019). Relatively diffuse molecular gas also show filamentary features, and such low-density, tenuous “striations” were first observed in CO lines (Goldsmith et al. 2008), and then seen in dust continuum with *Herschel* observations (Palmeirim et al. 2013).

There is growing evidence that filaments are not monolithic but have substructures. Hacar et al. (2013) identified multiple velocity components in position-position-velocity (PPV) space in the gas of the low-mass star-forming filament in Taurus, and suggested that the filament is indeed a bundle of those “velocity-coherent structures”, which are also termed “fibers”. After that work, similar fiber-like substructures have been detected in other dense, both low-mass and high-mass, molecular filaments (Henshaw et al. 2014; Fehér et al. 2016; Hacar et al. 2018; Shimajiri et al. 2019), while the physical origin of the fibers remains unclear (Tafalla & Hacar 2015; Clarke et al. 2017). The methodologies used to extract fibers (or fiber-like substructures) all work in PPV space, but vary in practice for the detailed techniques. There is caution that features identified in PPV space do not really represent density structures in position-position-position (PPP) space (see Clarke et al. 2018), but this issue could be mitigated with interferometer high angular resolution observations which have started to spatially resolve the internal structure of a filament. Filament substructures may also play a role in the formation and dynamical evolution of hubs or ridges in massive HFSs. Henshaw et al. (2017) observed a protostellar hub within an massive infrared dark cloud with the Atacama Large Millimeter/submillimeter Array (ALMA) in the 1 mm continuum, and detected multiple intra-hub subfilaments, which are narrow (0.028 pc) and analogous to fibers. Hacar et al. (2018) identified dozens of dense fibers in the central region of the well-known Integral-Shape Filament (ISF) in Orion, and recognized multiple hub-like associations along a dense bundle of the fibers. Nevertheless, observational studies capable of resolving massive filaments and hubs are still very limited, leaving several key questions in the context unsolved: (1) what are the physical properties of the substructures in massive HFSs and how do they differ from their low-mass counterparts? (2) What a role do these substructures play in shaping the initial conditions of high-mass star and cluster formation? (3) How are they related to large-scale filaments connected to the peripherals of the hubs or ridges? To shed light on these questions, we carry out interferometer molecular spectral line observations toward the central ridge of a pronounced massive HFS, and successfully resolve its inner structures both spatially and kinematically. By deriving the physical properties of the substructures and investigating their kinematics and dynamics, we try to understand their relation with the ongoing high-mass star formation.

The DR21 ridge (also called DR21 filament) is an elongated massive gas structure connected by several filaments with varying orientations, forming a remarkable HFS in the Cygnus X molecular cloud complex (Motte et al. 2007; Schneider et al. 2010; Hennemann et al. 2012). It contains a massive clump in the southern end and a filamentary structure to the north. The southern clump is embedded with at least two compact H II regions, namely DR21 (Cyganowski et al. 2003). The filamentary structure in the north contains a chain of ~ 0.1 pc massive dense cores (MDCs), and the most massive one is DR21(OH), which is associated with various masers and actively forming a cluster of high-mass stars (Zapata et al. 2012). While the DR21 ridge in the literature refers to the whole structure including both DR21 and DR21(OH), in this work we only focus on the continuous structure in the north; we leave out the DR21 clump for its discontinuity with the northern part and its more advanced evolutionary stage (thus of less relevance to the initial conditions of high-mass star formation). And to avoid confusion, we refer to this structure as the “DR21(OH) ridge”. Located at a distance of 1.5 kpc (Rygl et al. 2012), this structure has a projected length of ~ 2.5 pc and a total gas mass of $\sim 9000 M_{\odot}$, making its line mass two orders of magnitude higher than those of the low-mass filaments (e.g. Hill et al. 2011; Hacar et al. 2013) and about 10 times higher than that of the ISF in Orion (Schuller et al. 2021). Given its relatively close distance and great mass, the DR21(OH) ridge is an ideal target for disentangling the substructures of high-mass cluster-forming HFSs.

2. OBSERVATIONS

The DR21(OH) ridge was observed in the 3 mm waveband, covering H^{13}CO^+ (1–0), N_2H^+ (1–0), and NH_2D ($1_{1,1} - 1_{0,1}$), with the 15-antenna Combined Array for Research in Millimeter-wave Astronomy (CARMA) in the D configuration during June 29–July 14, 2014 (Project ID: c1212; PI: Keping Qiu). The CARMA D array provides a baseline range of 11–148 m, yielding a synthesized beam size of $\sim 5''$ (0.036 pc@1.5 kpc) and a largest recovering scale of $\sim 70''$ (0.5 pc@1.5 kpc). Mosaic observations toward four phase centers (R.A.=20^h39^m01^s.0; Decl.=42°22'25".5, 42°23'25".5, 42°24'25".5, and 42°25'25".5) were conducted to map the ridge. Observations toward each phase center were made with one or two scheduling blocks, leading to a total observing time of about 5 to 6 hours and an on-source integration time of 2 to 3 hours each. Spectral windows #7, #4, and #8 of the CARMA correlator were centered at the rest frequencies of the H^{13}CO^+ , N_2H^+ , and NH_2D transitions, respectively, with a uniform bandwidth of 31.152 MHz and spectral resolution of 97.7 kHz (0.33 km s⁻¹@90 GHz; 319 channels). J1927+739 was used as the bandpass calibrator and MWC349 was used for both flux calibration and time-dependent phase and amplitude

gain calibration. The raw data were flagged, calibrated, and imaged with the Miriad software (Sault et al. 1995). We used the Briggs weighting with the robust parameter set to 0.5 to image the data. The final data products contain three mosaic spectral line cubes with a map size of about $3' \times 6'$ and a pixel size of $1''.5$. The velocity resolutions are 0.34, 0.31, and 0.34 km s^{-1} , and the $1-\sigma$ noise levels are 36.9, 42.4, and 34.7 mJy beam^{-1} per velocity channel for the H^{13}CO^+ , N_2H^+ , and NH_2D data cubes, respectively. Detailed observational setups and logs can be found at the CARMA Data Archive¹.

3. RESULTS, ANALYSIS, AND DISCUSSION

Figure 1 shows the velocity channel maps of the H^{13}CO^+ ($1-0$) emission, where the original channel width of 0.34 km s^{-1} is smoothed to 1.0 km s^{-1} . The H^{13}CO^+ emission is detected at -6 to 1 km s^{-1} , with the emission at $\lesssim -3.0 \text{ km s}^{-1}$ mostly traces the high density peaks as visualized by a chain of active MDCs (Motte et al. 2007). On the other hand, the emission at $\gtrsim -2.0 \text{ km s}^{-1}$ reveals new features to the west of the MDC chain. Overall the results here are consistent with the single-dish H^{13}CO^+ ($1-0$) observations by Schneider et al. (2010), except that our data have a factor of 6 better angular resolution. Because of the missing zero-spacing information, our interferometer observations filter out extended emission (larger than 0.5 pc, see Section 2). We anticipate, however, that the extraction and analysis of the substructures within the DR21(OH) ridge are not strongly affected. We do not show the velocity channel maps in N_2H^+ ($1-0$) and NH_2D ($1_{1,1}-1_{0,1}$), since these transitions have blended hyperfine lines. The velocity-integrated emissions of the three lines are all highly biased to the structure coincident with the MDC chain (Figure 2). Thus, more sophisticated analyses of the spectral line data are needed to better unraveling the velocity structure of the ridge (see Section 3.2).

3.1. High-resolution H_2 Column Density Map and Dust Temperature Map Derived from Continuum Data

To calculate the mass and other physical properties, high-resolution ($13''.7$) H_2 column density (N_{H_2}) and dust temperature (T_{dust}) maps of the DR21(OH) ridge are derived by fitting the dust continuum emissions at submillimeter wavelengths with a modified blackbody model (Hildebrand 1983):

$$I_{\nu} = B_{\nu}(T_{\text{dust}})(1 - e^{-\tau_{\nu}}), \quad (1)$$

$$\tau_{\nu} = \mu_{\text{H}_2} m_{\text{H}} N_{\text{H}_2} \kappa_{\nu} / \Gamma, \quad (2)$$

where $B_{\nu}(T_{\text{dust}})$ is the Planck function, $\mu_{\text{H}_2} = 2.8$ is the mean molecular weight per H_2 molecule, m_{H} is the mass of the hydrogen atom, κ_{ν} is the dust mass opacity, and $\Gamma = 100$ is a canonical gas-to-dust mass ratio for the interstellar medium. We evaluate κ_{ν} following $\kappa_{\nu} = \kappa_0 (v/v_0)^{\beta}$, where $\kappa_0 = 10 \text{ cm}^2 \text{g}^{-1}$, $v_0 = 1 \text{ THz}$, and $\beta = 2$. This dust opacity law is widely used by the *Herschel* large survey projects (e.g., André et al. 2010; Tigé et al. 2017). The continuum maps used for the fitting were obtained from Cao et al. (2019) which include the *Herschel*/PACS 160 μm map and the James Clerk Maxwell Telescope (JCMT)/SCUBA-2 450 and 850 μm maps. The beam sizes of the 160, 450, and 850 μm maps are $12''.6$, $7''.9$, and $13''$, respectively. We did not use the *Herschel* 70 μm data due to the possible contaminations from the emissions of very small grains (Draine & Li 2001) that are not considered in the single-temperature model (see Figure 12 of Cao et al. 2019). The *Herschel* maps at 250, 350, and 500 μm were not used since their resolutions are too coarse ($> 18''$) compared with the CARMA data. The continuum maps used for the fitting were cropped to the same size as the CARMA data ($3' \times 6'$), smoothed to a common beam size of $13''.7$, and resampled to the same gridding with a pixel size of $2''$. The flux uncertainties of the continuum maps are conservatively estimated to be 20% following Cao et al. (2019) and are considered in the fitting procedure. We use the *minimize* function in the Scipy² (Jones et al. 2001) package to implement the fitting. The derived N_{H_2} map is shown in Figures 1 and 2, and the T_{dust} map is shown in Figure 2 (also see the N_{H_2} and T_{dust} uncertainties in Appendix A). To test the robustness of the results derived from the 3-band fitting, we generate another set of N_{H_2} and T_{dust} maps with 6-band data (*Herschel* 160, 250, 350, and 500 μm ; JCMT 450 and 850 μm) and compare them at the same resolution (see Appendix A). We find that 93% of the total map area has T_{dust} differences less than 2 K, and 90% of the map area has relative differences in N_{H_2} less than 25%, indicating that the 3-band fitting is robust.

N_{H_2} and T_{dust} in the DR21(OH) ridge range from 5×10^{21} to $1 \times 10^{24} \text{ cm}^{-2}$ and from 15 to 31 K, respectively, where the highest column density and temperature are both found toward the DR21(OH) core. The ridge can be defined with a N_{H_2} contour level of 10^{23} cm^{-2} as suggested by Hennemann et al. (2012). In Figure 1, if we define the outer edge of the ridge with a slightly lower N_{H_2} value of $5 \times 10^{22} \text{ cm}^{-2}$, the H^{13}CO^+ emissions, including the bright emission tracing the MDC chain and the new features to the west, are all confined to be within the ridge. In Figure 2(a), to the west of the MDC chain, the 8 μm dark patches (absorption)

¹ <http://carma-server.nsa.uiuc.edu:8181/>

² <https://www.scipy.org/>

coincident with the H^{13}CO^+ emission features are also perceptible. All this indicates that H^{13}CO^+ emission is probing high density substructures within the DR21(OH) ridge.

3.2. Spectral Fitting and the PPV Structures of the DR21(OH) ridge

To exact the PPV structures and derive the physical properties of the DR21(OH) ridge, we fit the data cubes of the three transitions pixel-by-pixel with a multi-velocity-component spectral line model based on the theoretical work of [Mangum & Shirley \(2015\)](#). In this model, the i th velocity component along the line-of-sight (LoS) of a pixel has a total column density $N_{\text{trc},i}$ for a certain tracer and an excitation temperature T_{ex} . From Eq. (32) of [Mangum & Shirley \(2015\)](#), we have the velocity distribution of the tracer column density

$$N_{\text{trc},i}(v) = \frac{3h}{8\pi^3 S \mu^2} \frac{Q_{\text{rot}}}{g_u} e^{\frac{E_u}{k_B T_{\text{ex}}}} \left(e^{\frac{h\nu_0}{k_B T_{\text{ex}}}} - 1 \right)^{-1} \tau_{vi}(v), \quad (3)$$

where h is the Planck constant, k_B is the Boltzmann constant, and S , μ , g_u , Q_{rot} , E_u , ν_0 are the line strength, dipole moment, degeneracy of the upper energy level, rotational partition function, upper level energy, and rest frequency of the transition, respectively. We assume in the model that $N_{\text{trc},i}(v)$ has a Gaussian distribution with a centroid velocity ν_{0i} and a velocity dispersion σ_{vi} , leading to

$$N_{\text{trc},i}(v) = \frac{N_{\text{trc},i}}{\sqrt{2\pi}\sigma_{vi}} e^{-\frac{(v-\nu_{0i})^2}{2\sigma_{vi}^2}}. \quad (4)$$

Further taking into account hyperfine lines for a transition, we derive the opacity of the j th hyperfine line of a transition for the i th velocity component

$$\tau_{vij}(v) = \frac{4\sqrt{2\pi^5} S \mu^2 R_j g_u}{3h Q_{\text{rot}} \sigma_{vi}} N_{\text{trc},i} \left(e^{\frac{h\nu_0}{k_B T_{\text{ex}}}} - 1 \right) e^{-\frac{(v-\nu_{0i}-\delta\nu_j)^2}{2\sigma_{vi}^2} - \frac{E_u}{k_B T_{\text{ex}}}}, \quad (5)$$

where R_j and $\delta\nu_j$ are the relative line strength and the velocity offset relative to ν_0 for the j th hyperfine line, respectively. Here we assume that all the velocity components along the LoS of one pixel have a common T_{ex} , otherwise the radiative transfer equation is not analytically integrable and the detailed material distribution along the LoS must be known. The modeled spectral intensity as a function of velocity is given by

$$\Delta I_V(v; N_{\text{trc},i}, T_{\text{ex}}, \nu_{0i}, \sigma_{vi}) = (B_V(T_{\text{ex}}) - B_V(T_{\text{bg}})) \left(1 - e^{-\sum_{ij} \tau_{vij}(v)} \right), \quad (6)$$

where T_{bg} is the background brightness temperature and is set to the cosmic microwave background value of 2.73 K. Note that this spectral model is quite general and does *not* rely on additional assumptions such as the Rayleigh-Jeans approximation or the optically thin approximation. By fitting an observed spectrum with this model one can obtain a parameter set $(N_{\text{trc},i}, T_{\text{ex}}, \nu_{0i}, \sigma_{vi})$ for each velocity component toward a pixel.

Since we only have observations of one transition for one molecular species, T_{ex} and N_{trc} cannot be determined simultaneously in the fitting due to degeneracy. Therefore we fix T_{ex} to T_{dust} obtained in Sect. 3.1 for each pixel during the fitting procedure, by assuming that the gas and dust temperatures are equal. This assumption is valid if the gas and dust are strongly coupled (e.g., [Burke & Hollenbach 1983](#)). At low to intermediate densities ($n \lesssim 10^4 \text{ cm}^{-3}$), relatively weak gas-dust coupling and the depletion of coolant species may conspire a considerably higher gas temperature than the dust temperature; such an effect can be significantly reduced at higher densities thanks to rapid gas-dust coupling, leading to a temperature difference of ~ 4 K at $n \sim 10^5 \text{ cm}^{-3}$ and completely negligible at $n \sim 10^6 \text{ cm}^{-3}$ ([Goldsmith 2001](#)). Dust evolution in dense cores can affect thermal gas-dust coupling, leading to a higher gas temperature compared to the dust temperature, but the temperature difference is also small at high densities (~ 3 K at $n \sim 10^5 \text{ cm}^{-3}$ and ~ 1 K at $n \sim 10^6 \text{ cm}^{-3}$, [Ivlev et al. 2019](#)). In our case, we have gas densities $> 10^5 \text{ cm}^{-3}$ (N_{H_2} in Figure 1 divided by 0.1 pc, which is derived in Sect. 3.4, also see Table 1). Thus the dust temperature approximates the gas temperature within a few K. We further assess in Appendix B that a small variation of 4 K in T_{ex} induces a 12% difference in the fitted $N_{\text{trc},i}$. We use the tool *curve_fit* in Scipy to extract and fit 7,625, 7,500, and 2,141 spectra and obtain a total of 10,152, 7,766, and 2,141 velocity components for the transitions of H^{13}CO^+ , N_2H^+ , and NH_2D , respectively (note that one pixel can have multiple velocity components). These velocity components can be identified as points in the PPV space (hereafter ‘‘PPV points’’). Figure 3 provides 2D views of the PPV points. While projected on the plane of sky (PoS), these PPV points are grouped into several fiber-like substructures which entangle around the DR21(OH) core and branches to

the north (Figures 3(a–c)). In the position-velocity (PV) diagrams (Figures 3(d–f)), the PPV points exhibit complicated velocity structures, which might be a consequence of supersonic turbulence. A particular interesting feature seen in the H^{13}CO^+ emission is the westernmost “branch” in Figure 3(a); we will come back to this substructure later by modeling its PV structure as revealed in Figure 3(d).

3.3. Identification of the Fibers

To identify the fibers seen in the PPV space, we apply the agglomerative clustering implementation in the scikit-learn package³ (Pedregosa et al. 2011) to the PPV points for each transition. The agglomerative clustering algorithm groups points in N -dimensional space via recursively merging points or clusters (i.e. groups of points) into higher-order clusters such that the pair of points or clusters to be merged minimally increases the linkage distance (Ward 1963). To make the clustering procedure adjustable, we introduce two parameters t_x and t_v in defining the linkage distance of two PPV points:

$$s_{\text{link},ij} = \sqrt{[t_x(x_i - x_j)]^2 + (y_i - y_j)^2 + \left(\frac{v_i - v_j}{t_v}\right)^2}, \quad (7)$$

where x and y are the spatial coordinates in *physical* units, and v is the LoS velocity. For each transition, we adjust the parameters (t_x , t_v) and run the algorithm with the modified coordinates of the PPV points as input. By practice we found that the best values of (t_x , t_v) for identifying the fiber structures in the H^{13}CO^+ , N_2H^+ , and NH_2D data are (2.8 pc, $1.0 \text{ km s}^{-1} \text{ pc}^{-1}$), (0.5 pc, $0.8 \text{ km s}^{-1} \text{ pc}^{-1}$), and (1.0 pc, $2.0 \text{ km s}^{-1} \text{ pc}^{-1}$), respectively, with which the DR21(OH) ridge is decomposed into 3, 3, and 2 fibers in the PPV space. Figure 4 shows the identified fibers projected on the PoS and their PV plots, with the color coding representing different velocities. In the H^{13}CO^+ data, three fibers with roughly north-south orientations are clearly seen; these fibers have distinct velocities, forming a “trident” with the junction approximately coincident with the DR21(OH) core. We name the three fibers as f1, f2, and f3 from east to west. Among the fibers, f1 is clearly tracing the central densest part of the dust ridge well known from previous dust continuum observations (Motte et al. 2007; Hennemann et al. 2012); f2 and f3 are relatively new, not seen in the dust emission, but previous single-dish H^{13}CO^+ ($1-0$) observations showed that the ridge slight moves from east to west with the velocity increasing from -5 km s^{-1} to 0 km s^{-1} (Schneider et al. 2010), in a manner consistent with the positions and velocities of the three fibers identified here. In particular, f3 is also discernible in the H^{13}CO^+ ($1-0$) map in Schneider et al. (2010) (see their Figure 9), though at a much lower resolution. Given the LoS velocities of the fibers and the existing observations suggesting that the DR21(OH) ridge is in global collapse (Schneider et al. 2010), one may expect that f1 and f3 are on the far side and the near side along LoS, respectively, and that f2 is probably in the middle. The three fibers in the N_2H^+ line are less prominent yet are still clearly seen with positions and velocities consistent with those in the H^{13}CO^+ line, indicating that they are tracing the same physical entities. While the whole f1 and the southern part of f3 are detected, f2 is fragmented into several parts, probably due to the regional variations of the abundances of the two molecular tracers. On the other hand, in the NH_2D line, the whole f1 (though fragmented into to parts) and the northern part of f2 are detected, and f3 is completely absent. The appearance of the fibers are also different from that in the H^{13}CO^+ and N_2H^+ lines by their more compact morphologies and smaller widths. In addition, in contrast to what is seen in the H^{13}CO^+ and N_2H^+ lines, the southern end of f1 in the NH_2D line is shifted to the west and does not coincide with the DR21(OH) core, indicating that active high-mass star formation has destroyed most of NH_2D . The detection information of the fibers in the three transitions is summarized in Table 1.

3.4. Characterizing the Properties of the Fibers

In this subsection we derive the physical properties of the fibers with the H^{13}CO^+ data due to their best detections. We first determine the major axes of the fibers in the PoS through linear regression analyses of the coordinates of the PPV points, and divided the PPV points of each fiber into 15 equal-length parts along the major axis. For each part a “bone” point is generated with flux-weighted mean positions and other physical parameters (N_{trc} , T_{ex} , v_0 , σ_v) of the PPV points in that part. The derived bone points of the three fibers are shown in Figure 4, which delineate the axes of the fibers in the PPV space and can be used for calculating the distribution of the physical properties along the fibers. Lengths of the fibers are estimated as the lengths of the bone lines, and the widths are evaluated as the dispersions of the distances of the PPV points to the bone lines. Other physical quantities (e.g. the mean LoS velocity and velocity dispersion) of a fiber are derived as intensity-weighted averages over all the PPV points belonging to the fiber. Similarly, profiles of a physical quantity along the fibers can be calculated as the intensity-weighted averages over the PPV points with which the bone points are derived. Table 1 lists the geometric and physical parameters of the fibers.

³ <https://scikit-learn.org/stable/>

To estimate the total gas masses of the fibers we need a conversion factor from N_{trc} to N_{H_2} , i.e. the abundance. This is done by comparing N_{trc} obtained from the spectral fitting with N_{H_2} derived from the dust continuum emissions. We use the H^{13}CO^+ data to derive the total mass since its emission matches the N_{H_2} map the best among the three species (see Figure 2). A map of the H^{13}CO^+ column density is generated with the PPV points and was smoothed and resampled to match the resolution and gridding of the N_{H_2} map. An abundance map is then derived by dividing the $N_{\text{H}^{13}\text{CO}^+}$ map with the N_{H_2} map. The resultant mean abundance for H^{13}CO^+ in the DR21(OH) ridge is 1.72×10^{-10} with a regional fluctuation of ~ 0.25 dex. In addition, we find that there is no strong correlation between the H^{13}CO^+ abundance and T_{dust} or N_{H_2} (see Appendix B for detailed analyses), which indicates that the H^{13}CO^+ abundance does not vary violently with the differentiated chemical conditions (e.g. depletion onto dust grains and formation/destruction through chemical reactions) and that adopting a constant abundance value is sufficient for calculating the mass. By converting $N_{\text{H}^{13}\text{CO}^+}$ to N_{H_2} with this abundance we derive that the total masses of fibers f1, f2, and f3 to be 5117, 1838, and 921 M_{\odot} , respectively, and the line masses are 2133, 795, and 511 $M_{\odot} \text{ pc}^{-1}$, respectively, which is 1–2 orders of magnitude higher than typical low-mass filaments (e.g. Pezzuto et al. 2020). See also Table 1 for more details on the physical properties of the fibers.

3.5. Free-fall Velocity Profile seen in Fiber f3

One of the most prominent features of the DR21(OH) ridge in the PPV space is the large velocity gradient in fiber f3, which is clearly seen in the PV diagrams of the H^{13}CO^+ and N_2H^+ emissions (Figure 3). This velocity gradient is not constant throughout the fiber, but increases from north to south, i.e., toward the direction of DR21(OH). In addition, the FWHM velocity dispersion of f3 increases almost monotonously from 0.3 to 1.9 km s^{-1} from north to south as seen in the H^{13}CO^+ data. These suggest that f3 is very likely influenced by the gravitational potential of the very massive dense core and the gas within the fiber is falling towards DR21(OH). Schneider et al. (2010) made a similar statement based on the emission distribution revealed by their single-dish observations. Here the data with a much higher angular resolution allow us to further test this interpretation, and we fit the PV pattern with a free-fall model. The PPV points used in the fitting are highlighted in Figure 3. Based on the morphologies and spatial configuration of f3 and DR21(OH), we assume that f3 is falling directly toward DR21(OH) with no transverse motions and that the free-fall velocity is zero at infinity. In the 3D space, the free-fall velocity v_{ff} as a function of the distance to the mass center l is

$$v_{\text{ff}}(l) = \sqrt{\frac{2GM_{\text{c}}}{l}}, \quad (8)$$

where M_{c} is mass of the gravity center. Since we can only observe LoS velocity and the projected distance on the PoS Eq. 8 can be rewritten in a “projected” form that implicitly contains the inclination angle:

$$v_{\text{LoS}}(l_{\text{p}}) = \sqrt{\frac{2GM_{\text{c,p}}}{l_{\text{p}}}} + v_{\text{c,LoS}}, \quad (9)$$

where $l_{\text{p}} = l \cos \theta_{\text{inc}}$ and $M_{\text{c,p}} = M_{\text{c}} \cos \theta_{\text{inc}} \sin^2 \theta_{\text{inc}}$ are the “projected” distance and mass, respectively, θ_{inc} is the inclination angle of f3 against the PoS, and $v_{\text{c,LoS}}$ is the systematic LoS velocity of the gravity center. Since θ_{inc} is unknown we use the above equation to fit the velocity profile. The PPV points used for the fitting and the results are shown in Figure 3(g), which yield $M_{\text{c,p}} = 582.1 \pm 13.9 M_{\odot}$ and $v_{\text{c,LoS}} = -3.87 \pm 0.04 \text{ km s}^{-1}$. The $v_{\text{c,LoS}}$ value is well consistent with the results derived from single-dish spectral line observations toward DR21(OH) (Mayer et al. 1973; Chandler et al. 1993). The value of $M_{\text{c,p}}$ is compatible with the mass of DR21(OH) (446–1048 M_{\odot} , Motte et al. 2007; Cao et al. 2019), but since it is only the lower limit of the mass of the gravity center, it does not rule out the possibility that other MDCs around DR21(OH) also contribute to the gravitational attraction. We stress that the observations and fitting results all support a scenario that the gas in f3 is falling toward DR21(OH), and the latter seems to be the main (but not necessary the only) source of gravitational attraction. The mass accretion rate of f3 can be estimated by multiplying the line mass and the infall velocity, which is taken from the free-fall model (4.9 km s^{-1} without accounting for the projection effect; see Figure 3(g)), and is $\gtrsim 2.5 \times 10^{-3} M_{\odot} \text{ yr}^{-1}$, indicating that a mass feeding through f3 is capable of significantly increasing the core mass within a free-fall time (typically 10^5 yr for dense cores) and thus play an important role in the high-mass and cluster formation within and around DR21(OH).

3.6. Instability of the fibers and the star formation in the DR21(OH) ridge

In this section we study the instability of the fibers and its relation to the star formation in this region. There are two modes of instabilities for a self-gravitating and isothermal gas cylinder: radial instability and axial instability. For the former, the critical line mass of a cylinder over which gravity overcomes supports of turbulence and thermal pressure is given by

$$\lambda_{\text{cr,radial}} = \frac{2\sigma^2}{G}, \quad (10)$$

where σ is the sound speed for thermal support and velocity dispersion in case of turbulent support (Ostriker 1964; Fiege & Pudritz 2000). The fibers mostly fall in a temperature range of 15 to 25 K (Figure 2(c)), so they are mildly supersonic with the velocity dispersions about 2 times the sound speed, leading to turbulent support. We then derive the critical line masses of 157, 182, and 130 $M_{\odot} \text{ pc}^{-1}$ for fibers f1, f2, and f3, respectively, which are only 7.3%, 23%, and 25% of their actual line masses (see Table 1). This indicates that the fibers are unstable against radial gravitational collapse with the turbulent (and thermal) support. We further derive the line mass and critical line mass profiles along the fibers derived with the statistics of the bone points, and find that the line masses are ~ 10 times larger than the critical values for most parts of the fibers (Figure 5). To estimate the relative importance of magnetic fields in the radial instability, we derive the magnetic energy, E_B , and the gravitational binding energy, E_G , of the fibers:

$$E_B = \frac{\pi}{4} d^2 L \cdot \frac{\bar{B}}{2\mu_0} = \frac{\pi^3}{32\mu_0} \bar{B}_{\text{PoS}}^2 d^2 L, \quad (11)$$

$$E_G = \frac{GM^2}{(d^2 L)^{1/3}}, \quad (12)$$

where μ_0 is the vacuum permeability, and d , L , M , \bar{B} , \bar{B}_{PoS} are the FWHM width, length, mass, average magnetic field strength, and average projected magnetic field strength on the PoS of a fiber, respectively. For \bar{B}_{PoS} we adopt the value in Girart et al. (2013) (0.62 mG) derived from the JCMT observations. The resultant gravitational binding energies are 7.0×10^{48} , 9.5×10^{47} , and 2.9×10^{47} erg, for fibers f1, f2, and f3, respectively, and the magnetic energies are 2.9×10^{46} , 2.5×10^{46} , and 1.3×10^{46} erg, which are only 0.4%, 2.6%, and 4.5% of the gravitational energies, respectively.

The axial instability (also known as the ‘‘sausage’’ instability) of a gas cylinder describes its mass agglomeration along the axial due to the growth of unstable perturbations. For such an instability there exists a characteristic length scale, $L_{\text{max,axial}}$, delineating the nearly uniform spacing between the fragments, as a result of the fastest growing unstable perturbation (Nagasawa 1987; Jackson et al. 2010). Nagasawa (1987) find that for a self-gravitating isothermal cylinder, $L_{\text{max,axial}} \sim 22H$, where $H = c_s(4\pi G\rho_c)^{-1/2}$ is the scale height, ρ_c is the density at the center of the cylinder, and that this length scale does not change with the presence of an axial magnetic field. With the analytical solution for hydrostatic equilibrium in a self-gravitating isothermal cylinder (Ostriker 1964), we derive a relation between the FWHM width d and the scale height as $d = 4.336H$, and find that $L_{\text{max,axial}} = 0.61$, 0.57, and 0.47 pc for f1, f2, and f3, respectively (see also Table 1). These length scales are ~ 4 times shorter than the fiber lengths and the fibers are thus axially unstable, which is consistent with the fragmented appearance of the fibers in Figures 2 and 4 and the oscillating line masses in Figure 5. In addition, the average separations of the line mass peaks (i.e. fragments) in Figure 5 are 0.54, 0.40, and 0.42 pc for f1, f2, and f3, respectively, which are in good agreement with their $L_{\text{max,axial}}$ considering the projection effect.

The analyses and results above all suggest that with the great line masses, gravity is playing a predominant role in shaping the dynamics of the fibers, and star formation is expected to happen in the fibers given their radial and axial instabilities. We use the catalogs of class II methanol masers and ultra-compact H II (UCH II) regions collected by Cao et al. (2019), as well as the MCDs with strong SiO emissions in Motte et al. (2007), to probe high-mass star-forming activities in the DR21(OH) ridge. To trace low-mass star formation we use the protostar catalogs in Davis et al. (2007) and Kryukova et al. (2014) generated with the *Spitzer* data. All these sources are shown in Figures 2–5. It is clear that f1 is active in high-mass star formation with a chain of active MDCs and UCH II regions (Kumar et al. 2007; Cao et al. 2019). And it is widely known that the DR21(OH) core, where the three fibers conjoin, is forming a cluster of high-mass stars (Zapata et al. 2012; Girart et al. 2013). The very active (high-mass) star-forming activities in the DR21(OH) ridge may be attributed to a global collapse of the HFS (see also Schneider et al. 2010). The morphology and kinematics of the three fibers identified here provide new insights into this scenario. The enhancement in N_{H_2} from north to south in the ridge (Figure 2(b)), the transverse velocity gradient of fibers, and the free-fall velocity profile seen in f3 are all consistent with a physical picture that the three fibers are colliding in the south and that high-mass star formation is enhanced in the colliding region. On the other hand, there is no significant star formation in the northern parts of f2 and f3, despite that they are still at least one order-of-magnitude more massive than low-mass star-forming filaments (e.g. Pezzuto et al. 2020). In light of the great masses of DR21(OH) and fiber f1, and the free-fall signature seen in f3, the disruptive tidal field in this region may act as a force against local gravity and inhibit the star formation (Renaud 2010; Li et al. 2016).

3.7. Fibers of the DR21(OH) ridge in a bigger picture: relation with the outer filaments

Besides the DR21(OH) ridge (or the DR21 ridge which includes the DR21 clump), another prominent feature of this massive HFS seen in the *Herschel* maps is the lower-density filaments connected to the ridge/hub. These filaments stretch in all directions, and are mostly gravitationally unstable to form fragments (i.e., filaments N, F1N, F1S, F3N, F3S, SW, and S in Hennemann et al. 2012), in contrast to the striations connected to low-mass filaments (Goldsmith et al. 2008; Palmeirim et al. 2013). Kinematic analyses using spectral observations show that these filaments are involved in the global collapse of the HFS and are probably feeding materials to the central regions (Schneider et al. 2010). In comparison, these filaments have lengths comparable to the fibers seen in the ridge, but their line masses are a factor of a few to 10 lower Hennemann et al. (2012); only the most massive filaments have masses and line masses comparable to those of the least massive fiber (f3).

One of the key questions regarding the outer filaments and inner fibers in this remarkable HFS is that whether the filaments are natural extensions of the fibers, or they are independent structures without actual connection. In Figure 6 we plot the bones of our fibers and of the seven filaments in Hennemann et al. (2012) overlaid on the N_{H_2} map of Cao et al. (2019). Apparently there are five filaments (N, F1N, F1S, F3N, and F3S) having potential connection with the fibers. Filament N seems to be the extension of fiber f1 in the map, yet there is possibility that it is instead the extension of fiber f2. Filaments F1N/F1S are more likely to be the extension of fiber f2, and single-dish ^{13}CO (1–0) observations in Schneider et al. (2010) (see their Fig. 3) show that F1N/F1S joins the ridge at velocities of -2 to -3 km s $^{-1}$, well matching the velocity of f2, further supporting that F1N/F1S is connected to f2. Schneider et al. (2010) suggested that F3 (resolved into F3N and F3S further out in Figure 6) is connected to a “sub-filament” seen in H^{13}CO^+ (1–0) (corresponding to our fiber f3). But F3N/F3S has a nearly east-west orientation whereas f3 is roughly in a north-south direction. There is also a velocity difference of 1–2 km s $^{-1}$ between the two structures. Moreover, with a clear identification of the fibers based on our high resolution observations and an improved picture of the outer filaments constructed with the *Herschel* data, the bones of the two structures do not connect with each other (Figure 6). Thus, it is more likely that f3 is an independent structure rather than being the inner part of F3.

Overall it appears that the filaments more parallel to the ridge (such as filaments N, F1N/F1S in Figure 6) are more likely to be the extensions of the inner fibers. This is consistent with a scenario that the large-scale filaments collide to form a ridge/hub, which will further grow in mass by gravitationally attracting the gas along the filaments, making the fibers in the ridge/hub more massive than the outer filaments. As the ridge/hub continues to gain mass, its gravitational well gets deeper and may attract new accretion flows with an even perpendicular orientation (such as filaments F3N/F3S in Figure 6). Future high resolution observations of massive HFSs covering both the hub/ridge and outer filaments may help to testify the above scenario and to advance our understanding of the initial conditions of high-mass star and cluster formation.

4. SUMMARY

We have observed the prominent DR21(OH) ridge in high-density tracing molecular spectral lines with the CARMA, and analyzed the data to extract the multiple velocity components, identified the fibers, and characterized the fiber properties, aimed at understanding the formation and evolution of the ridge and its relation to high-mass star and cluster formation. Our main findings are summarized below:

1. We clearly resolve the ridge into three fibers (f1, f2, and f3) which are not seen in existing (sub)millimeter continuum observations. The fibers have lengths around 2 pc, widths about 0.1 pc, and are mildly supersonic with velocity dispersions about 2 times the sound speed. They are nearly parallel in the north and conjoin in the south around the most massive and active star-forming core DR21(OH).
2. A velocity gradient increasing from north to south is clearly seen in f3, confirming previous single-dish observations (Schneider et al. 2010). We find that the velocity gradient can be well reproduced with a model of gas flow in free-fall and that the infall rate is $\gtrsim 2.5 \times 10^{-3} M_{\odot} \text{ yr}^{-1}$. Thus the materials in f3 seem to be falling toward DR21(OH) due to strong gravitational attraction from the MDC (and possibly other MDCs around as well), a scenario also proposed by Schneider et al. (2010).
3. The three fibers have line masses significantly larger than the critical value, and from the instability analyses, they are unstable against gravitational collapse both axially and radially. While the most massive fiber, f1, exhibits active high-mass star formation all the way from north to south, the other two fibers, f2 and f3, show essentially no star formation in their northern parts. Given the free-fall velocity field seen in fiber f3, gravitational tidal forces exerted by the massive materials in this region may account for some local inefficiency in star formation.

4. On larger scales, some of the peripheral filaments are likely to be the outer extensions of the fibers inside the ridge. By comparing the morphologies and masses between the peripheral filaments and the ridge fibers, we speculate that large filaments of more parallel orientations collide to form a HFS, and the central hub/ridge continues to grow in mass by gravitationally attracting the gas from the outer parts of the filaments, feeding the central colliding parts into massive fibers and promoting high-mass star and cluster formation. As the ridge gets more massive, its strong gravitational attraction may induce additional accretion flows of all the orientations.

ACKNOWLEDGMENTS

Y.C. and K.Q. are partially supported by National Key R&D Program of China No. 2017YFA0402600, and acknowledge the support from National Natural Science Foundation of China (NSFC) through grants U1731237 and 11629302. Y.C. acknowledges the funding supports from the Scholarship No. 201906190105 of the China Scholarship Council and from the Predoctoral Program of the Smithsonian Astrophysical Observatory (SAO). G.L. acknowledges the supports from Yunnan University grant C176220100028.

Facilities: Telescope

Software: Astropy(Astropy Collaboration et al. 2013), SciPy(Jones et al. 2001), scikit-learn(Pedregosa et al. 2011), MIRIAD(Sault et al. 1995)

Table 1. Properties of the fibers

Property	f1	f2	f3
H ¹³ CO ⁺ detection	Full	Full	Full
N ₂ H ⁺ detection	Full	Full	Southern part
NH ₂ D detection	Full	Northern part	None
Length (pc)	2.40	2.31	1.80
Width (pc)	0.12	0.11	0.09
v_{lsr} (km s ⁻¹)	-4.22	-2.28	-0.84
σ_v (km s ⁻¹)	0.58	0.62	0.53
Mass (M_{\odot})	5117	1838	921
λ (M_{\odot} pc ⁻¹)	2133	795	511
$\lambda_{\text{cr,radial}}$ (M_{\odot} pc ⁻¹) ^a	157	182	130
$L_{\text{max,axial}}$ (pc) ^b	0.61	0.57	0.47

^aCritical line mass for radial instability.

^bCharacteristic length scale for axial instability, also the wavelength of fastest growing perturbations.

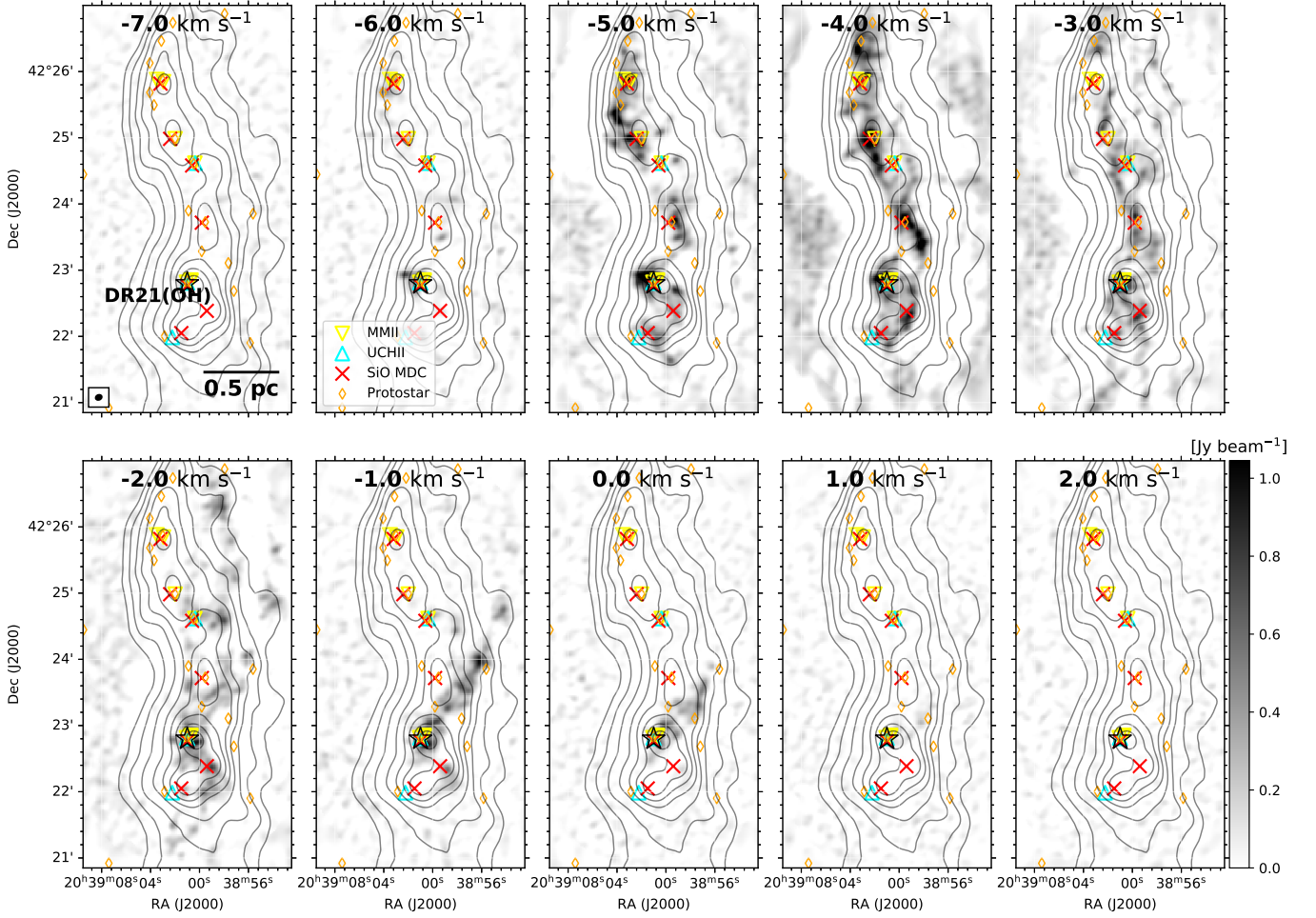


Figure 1. Channel maps of the H^{13}CO^+ ($1-0$) emission shown in gray scale, and the scaling is shown in a vertical bar in the lower-right corner. The central velocity of each channel is labeled on the top of each panel. Black contours of N_{H_2} in each panel derived with submillimeter continuum data (Sect. 3.1) are drawn at $1.5^{[0,1,2,3,\dots]} \times 5 \times 10^{22} \text{cm}^{-2}$. In all the panels, catalogs of class II methanol masers (MMII) and ultracompact H II (UC H II) regions are from Cao et al. (2019), and are marked as yellow inverted triangles and cyan triangles, respectively; massive dense cores with strong SiO emissions tabulated by Motte et al. (2007) are plotted as red crosses; protostars in Davis et al. (2007) and Kryukova et al. (2014) are marked as orange diamonds. The location of DR21(OH) is marked as a black star. A linear size scale bar and the CARMA beam are shown in the most upper left panel.

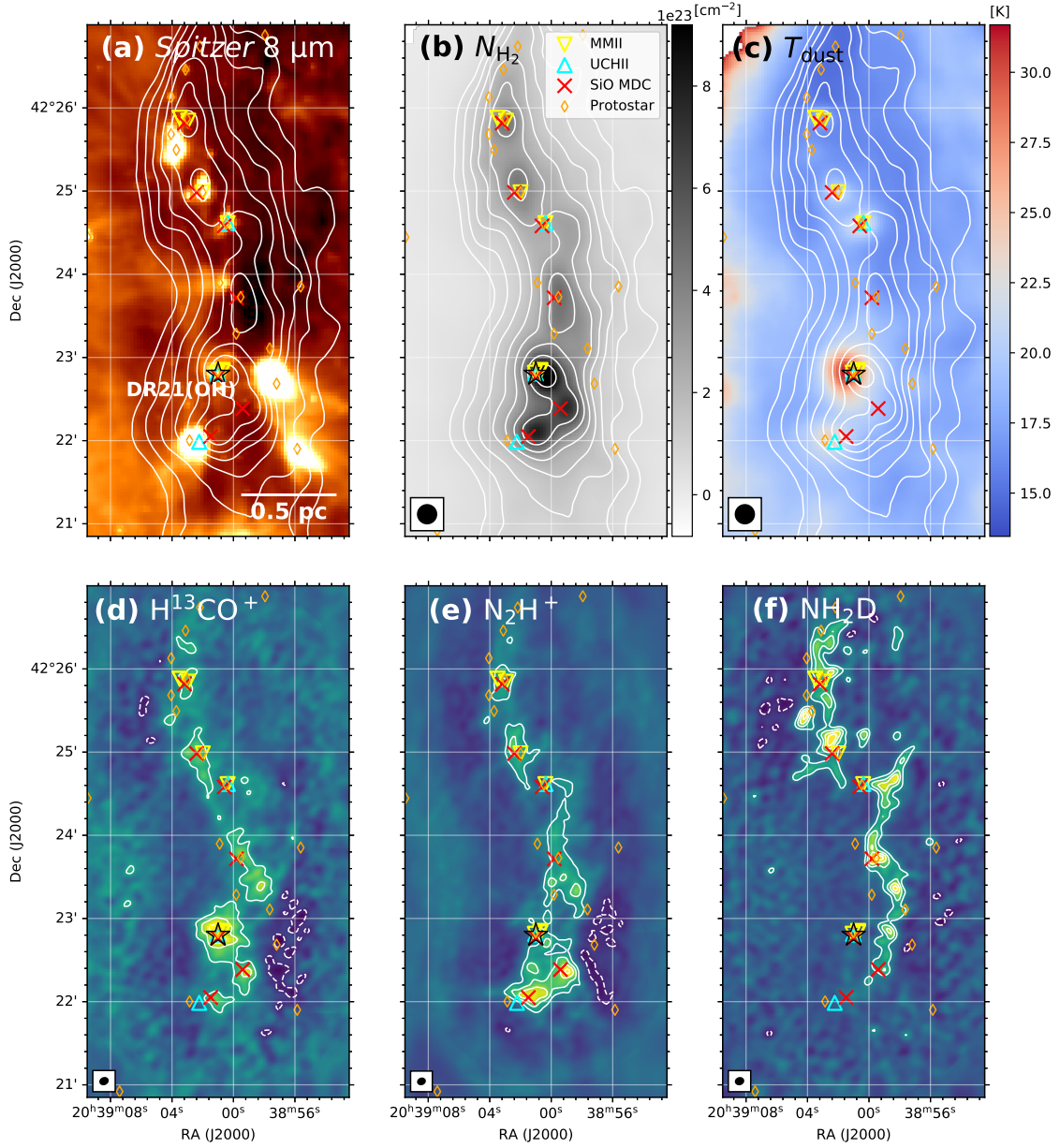


Figure 2. *Spitzer* 8 μm map (Panel a), high-resolution maps of N_{H_2} (Panel b) and T_{dust} (Panel c), and moment-0 maps of the three molecular transitions (Panels d–f) of the DR21(OH) ridge. White contours of N_{H_2} in Panels a–c are drawn with the same levels as those in Figure 1. Contours of the moment-0 maps in Panels d–f are drawn in $[\dots, -3, -2, -1, 1, 2, 3, \dots] \times \delta I$, where $\delta I = 1, 8,$ and $1 \text{ Jy beam}^{-1} \text{ km s}^{-1}$ for H^{13}CO^+ , N_2H^+ , and NH_2D , respectively, with negative contours shown as dashed curves. Other symbols in all the panels are the same as those in Figure 1.

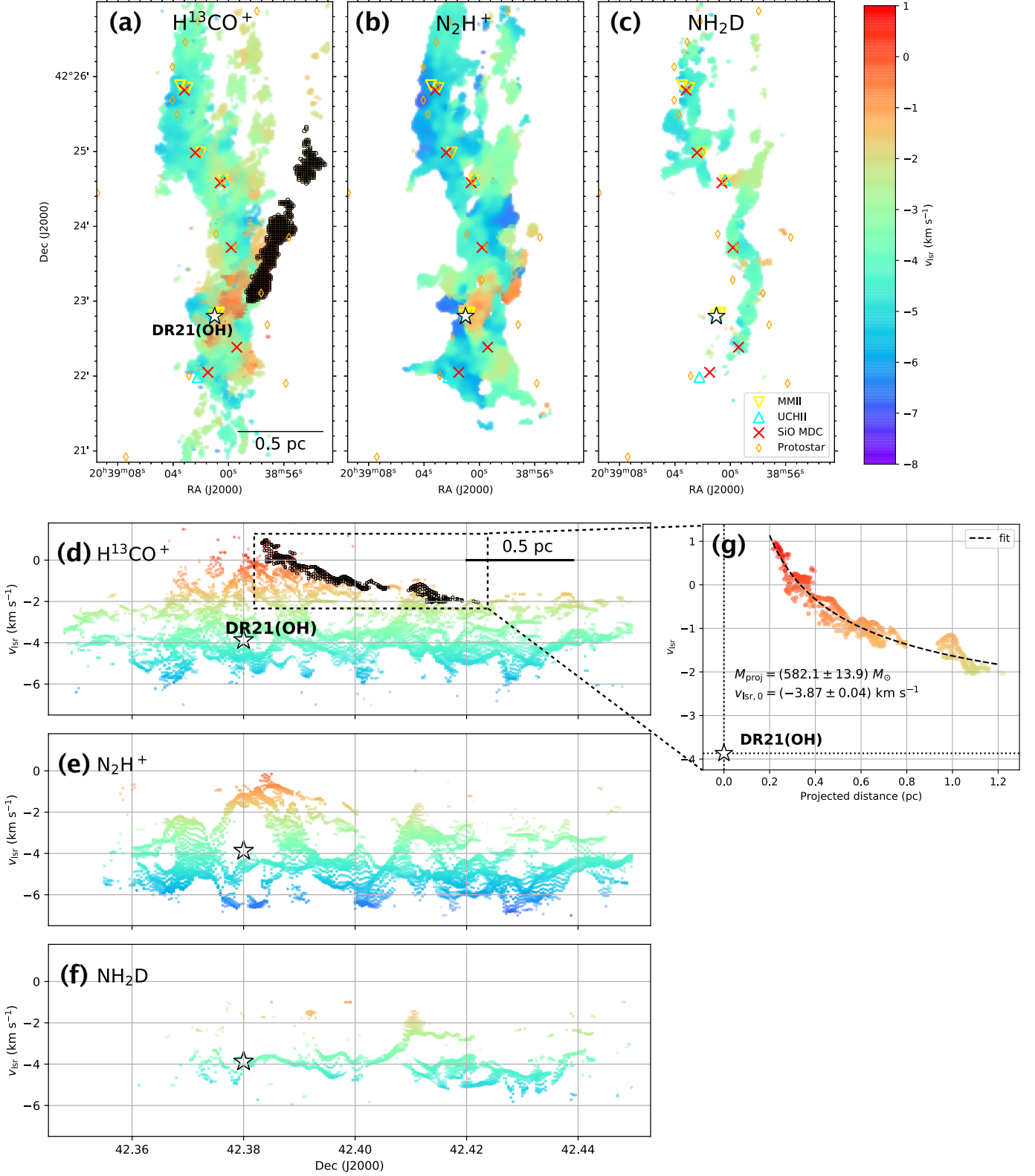


Figure 3. 2D views of the fitted velocity components (PPV points, see Sect. 3.2), which are shown in colored dots with the velocity color coding following a color bar to the top right. (a–c) PPV points (derived with the H^{13}CO^+ , N_2H^+ , and NH_2D spectra, respectively) placed on the plane of sky. (d–f) Position-velocity (PV) plots in the H^{13}CO^+ , N_2H^+ , and NH_2D lines, respectively, of the PPV points. Dots highlighted by black circles in Panels (a) and (d) denote the PPV points that are used for fitting a free-fall model shown as a dashed curve in Panel (g) (see Sect. 3.5 for details). Other symbols in all the panels are the same as shown in Figure 1.

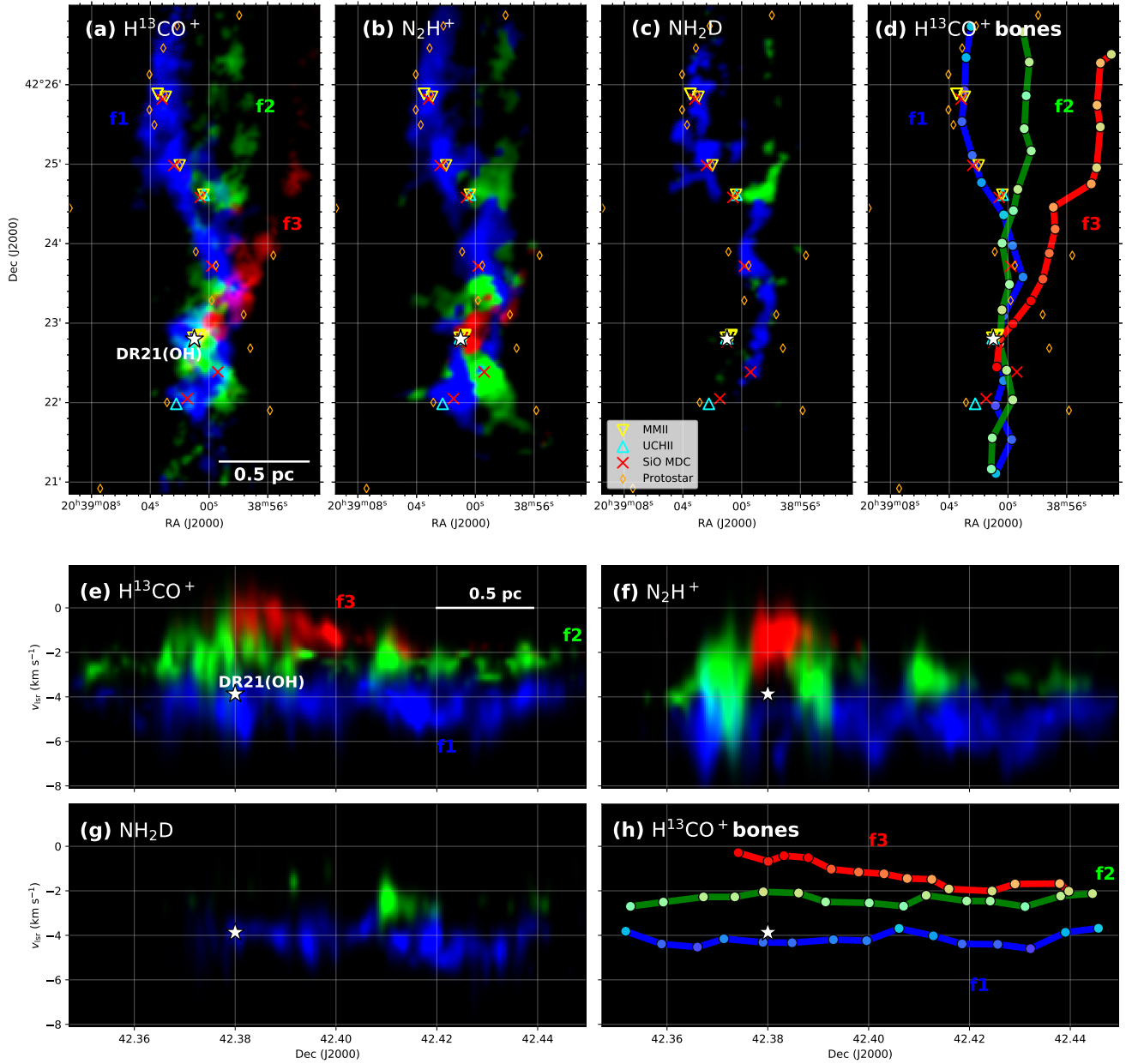


Figure 4. Panels (a–c) show the fibers, identified with the H^{13}CO^+ , N_2H^+ , and NH_2D spectra, respectively, as seen projected on the PoS; Panels (e–f) show the identified fibers in the H^{13}CO^+ , N_2H^+ , and NH_2D PV diagrams, respectively. The three fibers, f1, f2, and f3, are coded to blue, green, and red, respectively in all the panels, and the brightness in Panels (a–c) and (e–g) are proportional to the intensity that is derived from the spectral line fitting (Sect. 3.2). The bones of the fibers identified with the H^{13}CO^+ data are shown in Panels (d) and (h). The overlapping of the three bones in Panel (d) reflects their presumed positions along LoS, i.e. f1, f2, and f3 from far side to near side (Sect. 3.3). Other symbols in all the panels are the same as those in Figure 1.

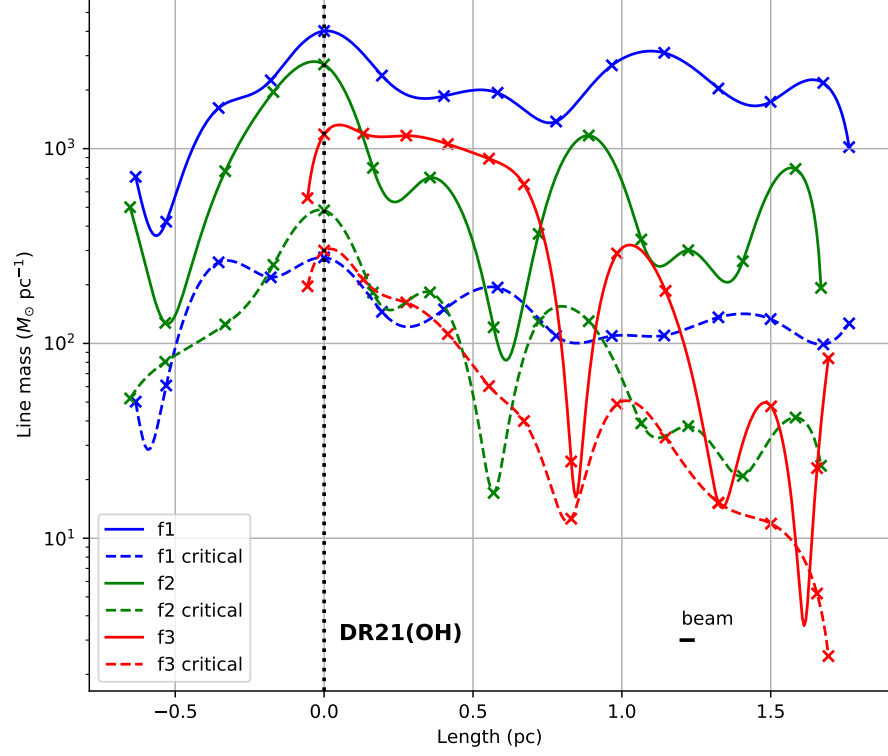


Figure 5. Line mass (solid lines) and critical line mass (dashed lines) profiles along the bones of the three fibers, derived with the H^{13}CO^+ data. The data points are marked as crosses and the lines are interpolations with order-3 splines. Critical line masses are derived with Eq. 10 and reflect the radial instability of the fibers (Sect. 3.6). All the profiles are aligned in position such that the origins are the closest bone points to DR21(OH). The CARMA beam is shown as a dash.

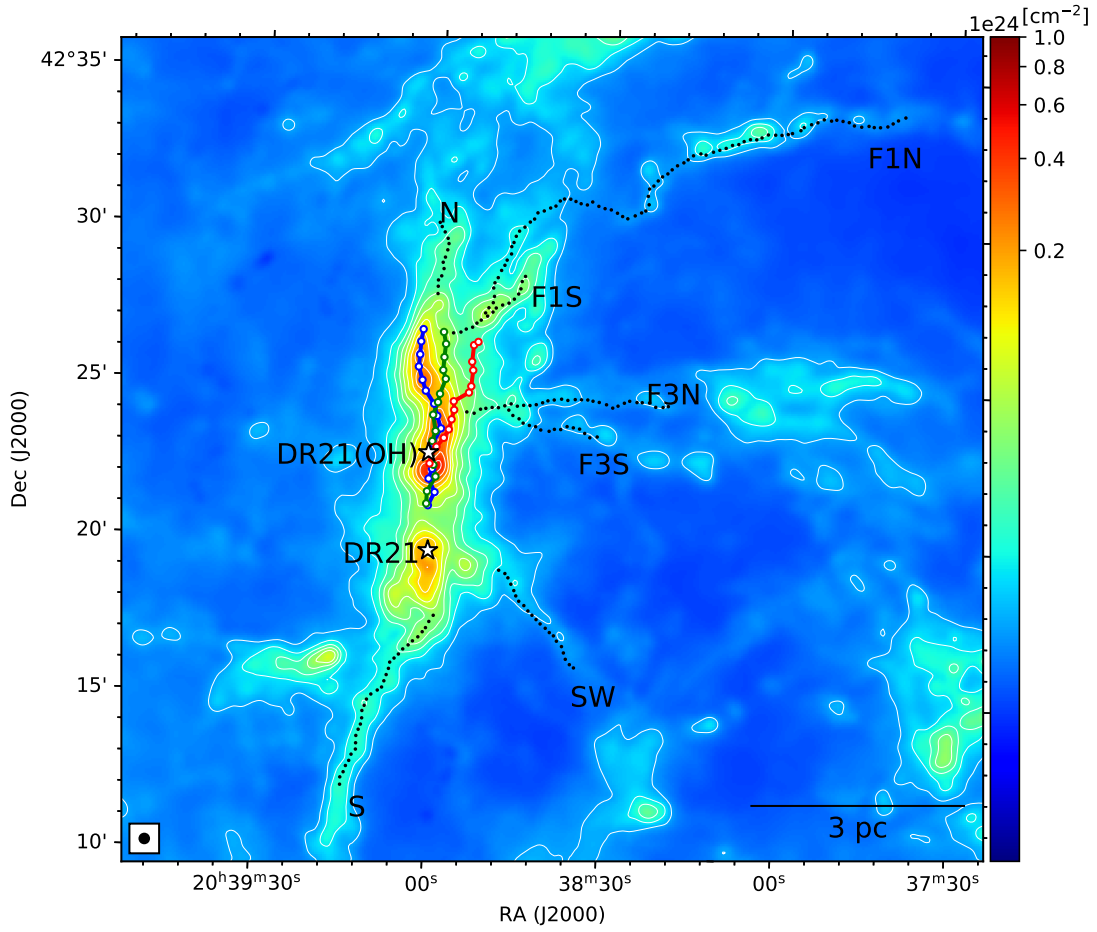


Figure 6. The N_{H_2} map derived by Cao et al. (2019) showing the DR21(OH) ridge and its large-scale environment. Contours of the N_{H_2} are drawn in $1.5^{[0,1,2,3,\dots]} \times 1.2 \times 10^{22} \text{ cm}^{-2}$. The bones of the three fibers in the DR21(OH) ridge are shown as blue, green, and red lines. Dotted lines outline the peripheral filaments in this region identified by Hennemann et al. (2012). The two most well-known MDCs, DR21 and DR21(OH), are marked as stars. Beam size of the map ($18'' \times 4''$) is shown in the lower-left corner.

REFERENCES

- André, P., Di Francesco, J., Ward-Thompson, D., et al. 2014, in *Protostars and Planets VI*, ed. H. Beuther, R. S. Klessen, C. P. Dullemond, & T. Henning, 27, doi: [10.2458/azu.uapress.9780816531240-ch002](https://doi.org/10.2458/azu.uapress.9780816531240-ch002)
- André, P., Men'shchikov, A., Bontemps, S., et al. 2010, *A&A*, 518, L102, doi: [10.1051/0004-6361/201014666](https://doi.org/10.1051/0004-6361/201014666)
- Araya, E. D., Kurtz, S., Hofner, P., & Linz, H. 2009, *ApJ*, 698, 1321, doi: [10.1088/0004-637X/698/2/1321](https://doi.org/10.1088/0004-637X/698/2/1321)
- Arzoumanian, D., André, P., Didelon, P., et al. 2011, *A&A*, 529, L6, doi: [10.1051/0004-6361/201116596](https://doi.org/10.1051/0004-6361/201116596)
- Astropy Collaboration, Robitaille, T. P., Tollerud, E. J., et al. 2013, *A&A*, 558, A33, doi: [10.1051/0004-6361/201322068](https://doi.org/10.1051/0004-6361/201322068)
- Burke, J. R., & Hollenbach, D. J. 1983, *ApJ*, 265, 223, doi: [10.1086/160667](https://doi.org/10.1086/160667)
- Busquet, G., Zhang, Q., Palau, A., et al. 2013, *ApJL*, 764, L26, doi: [10.1088/2041-8205/764/2/L26](https://doi.org/10.1088/2041-8205/764/2/L26)
- Cao, Y., Qiu, K., Zhang, Q., et al. 2019, *ApJS*, 241, 1, doi: [10.3847/1538-4365/ab0025](https://doi.org/10.3847/1538-4365/ab0025)
- Chandler, C. J., Moore, T. J. T., Mountain, C. M., & Yamashita, T. 1993, *MNRAS*, 261, 694, doi: [10.1093/mnras/261.3.694](https://doi.org/10.1093/mnras/261.3.694)
- Clarke, S. D., Whitworth, A. P., Duarte-Cabral, A., & Hubber, D. A. 2017, *MNRAS*, 468, 2489, doi: [10.1093/mnras/stx637](https://doi.org/10.1093/mnras/stx637)
- Clarke, S. D., Whitworth, A. P., Spowage, R. L., et al. 2018, *MNRAS*, 479, 1722, doi: [10.1093/mnras/sty1675](https://doi.org/10.1093/mnras/sty1675)
- Cyganowski, C. J., Reid, M. J., Fish, V. L., & Ho, P. T. P. 2003, *ApJ*, 596, 344, doi: [10.1086/377688](https://doi.org/10.1086/377688)
- Davis, C. J., Kumar, M. S. N., Sandell, G., et al. 2007, *MNRAS*, 374, 29, doi: [10.1111/j.1365-2966.2006.11163.x](https://doi.org/10.1111/j.1365-2966.2006.11163.x)
- Draine, B. T., & Li, A. 2001, *ApJ*, 551, 807, doi: [10.1086/320227](https://doi.org/10.1086/320227)
- Fehér, O., Tóth, L. V., Ward-Thompson, D., et al. 2016, *A&A*, 590, A75, doi: [10.1051/0004-6361/201424385](https://doi.org/10.1051/0004-6361/201424385)
- Fiege, J. D., & Pudritz, R. E. 2000, *MNRAS*, 311, 105, doi: [10.1046/j.1365-8711.2000.03067.x](https://doi.org/10.1046/j.1365-8711.2000.03067.x)
- Galván-Madrid, R., Zhang, Q., Keto, E., et al. 2010, *ApJ*, 725, 17, doi: [10.1088/0004-637X/725/1/17](https://doi.org/10.1088/0004-637X/725/1/17)
- Girart, J. M., Frau, P., Zhang, Q., et al. 2013, *ApJ*, 772, 69, doi: [10.1088/0004-637X/772/1/69](https://doi.org/10.1088/0004-637X/772/1/69)
- Goldsmith, P. F. 2001, *ApJ*, 557, 736, doi: [10.1086/322255](https://doi.org/10.1086/322255)
- Goldsmith, P. F., Heyer, M., Narayanan, G., et al. 2008, *ApJ*, 680, 428, doi: [10.1086/587166](https://doi.org/10.1086/587166)
- Hacar, A., Kainulainen, J., Tafalla, M., Beuther, H., & Alves, J. 2016, *A&A*, 587, A97, doi: [10.1051/0004-6361/201526015](https://doi.org/10.1051/0004-6361/201526015)
- Hacar, A., Tafalla, M., Forbrich, J., et al. 2018, *A&A*, 610, A77, doi: [10.1051/0004-6361/201731894](https://doi.org/10.1051/0004-6361/201731894)
- Hacar, A., Tafalla, M., Kauffmann, J., & Kovács, A. 2013, *A&A*, 554, A55, doi: [10.1051/0004-6361/201220090](https://doi.org/10.1051/0004-6361/201220090)
- Hennemann, M., Motte, F., Schneider, N., et al. 2012, *A&A*, 543, L3, doi: [10.1051/0004-6361/201219429](https://doi.org/10.1051/0004-6361/201219429)
- Henshaw, J. D., Caselli, P., Fontani, F., Jiménez-Serra, I., & Tan, J. C. 2014, *MNRAS*, 440, 2860, doi: [10.1093/mnras/stu446](https://doi.org/10.1093/mnras/stu446)
- Henshaw, J. D., Jiménez-Serra, I., Longmore, S. N., et al. 2017, *MNRAS*, 464, L31, doi: [10.1093/mnras/llw154](https://doi.org/10.1093/mnras/llw154)
- Hildebrand, R. H. 1983, *QJRAS*, 24, 267
- Hill, T., Motte, F., Didelon, P., et al. 2011, *A&A*, 533, A94, doi: [10.1051/0004-6361/201117315](https://doi.org/10.1051/0004-6361/201117315)
- Hollenbach, D. J., Takahashi, T., & Tielens, A. G. G. M. 1991, *ApJ*, 377, 192, doi: [10.1086/170347](https://doi.org/10.1086/170347)
- Hu, B., Qiu, K., Cao, Y., et al. 2021, *ApJ*, 908, 70, doi: [10.3847/1538-4357/abd03a](https://doi.org/10.3847/1538-4357/abd03a)
- Ivlev, A. V., Silsbee, K., Sipilä, O., & Caselli, P. 2019, *ApJ*, 884, 176, doi: [10.3847/1538-4357/ab4252](https://doi.org/10.3847/1538-4357/ab4252)
- Jackson, J. M., Finn, S. C., Chambers, E. T., Rathborne, J. M., & Simon, R. 2010, *ApJL*, 719, L185, doi: [10.1088/2041-8205/719/2/L185](https://doi.org/10.1088/2041-8205/719/2/L185)
- Jones, E., Oliphant, T., Peterson, P., et al. 2001, *SciPy: Open source scientific tools for Python*. <http://www.scipy.org/>
- Kirk, H., Myers, P. C., Bourke, T. L., et al. 2013, *ApJ*, 766, 115, doi: [10.1088/0004-637X/766/2/115](https://doi.org/10.1088/0004-637X/766/2/115)
- Krumholz, M. R., McKee, C. F., & Bland-Hawthorn, J. 2019, *ARA&A*, 57, 227, doi: [10.1146/annurev-astro-091918-104430](https://doi.org/10.1146/annurev-astro-091918-104430)
- Kryukova, E., Megeath, S. T., Hora, J. L., et al. 2014, *AJ*, 148, 11, doi: [10.1088/0004-6256/148/1/11](https://doi.org/10.1088/0004-6256/148/1/11)
- Kumar, M. S. N., Davis, C. J., Grave, J. M. C., Ferreira, B., & Froebrich, D. 2007, *MNRAS*, 374, 54, doi: [10.1111/j.1365-2966.2006.11145.x](https://doi.org/10.1111/j.1365-2966.2006.11145.x)
- Kumar, M. S. N., Palmeirim, P., Arzoumanian, D., & Inutsuka, S. I. 2020, *A&A*, 642, A87, doi: [10.1051/0004-6361/202038232](https://doi.org/10.1051/0004-6361/202038232)
- Li, G.-X., Burkert, A., Megeath, T., & Wyrowski, F. 2016, *arXiv e-prints*, arXiv:1603.05720. <https://arxiv.org/abs/1603.05720>
- Liu, H. B., Jiménez-Serra, I., Ho, P. T. P., et al. 2012, *ApJ*, 756, 10, doi: [10.1088/0004-637X/756/1/10](https://doi.org/10.1088/0004-637X/756/1/10)
- Mairs, S., Johnstone, D., Kirk, H., et al. 2015, *MNRAS*, 454, 2557, doi: [10.1093/mnras/stv2192](https://doi.org/10.1093/mnras/stv2192)
- Mangum, J. G., & Shirley, Y. L. 2015, *PASP*, 127, 266, doi: [10.1086/680323](https://doi.org/10.1086/680323)
- Mayer, C. H., Waak, J. A., Cheung, A. C., & Chui, M. F. 1973, *ApJL*, 182, L65, doi: [10.1086/181220](https://doi.org/10.1086/181220)
- Men'shchikov, A., André, P., Didelon, P., et al. 2010, *A&A*, 518, L103, doi: [10.1051/0004-6361/201014666](https://doi.org/10.1051/0004-6361/201014666)
- Molinari, S., Swinyard, B., Bally, J., et al. 2010, *A&A*, 518, L100, doi: [10.1051/0004-6361/201014659](https://doi.org/10.1051/0004-6361/201014659)
- Motte, F., Bontemps, S., & Louvet, F. 2018, *ARA&A*, 56, 41, doi: [10.1146/annurev-astro-091916-055235](https://doi.org/10.1146/annurev-astro-091916-055235)
- Motte, F., Bontemps, S., Schilke, P., et al. 2007, *A&A*, 476, 1243, doi: [10.1051/0004-6361:20077843](https://doi.org/10.1051/0004-6361:20077843)
- Myers, P. C. 2009, *ApJ*, 700, 1609, doi: [10.1088/0004-637X/700/2/1609](https://doi.org/10.1088/0004-637X/700/2/1609)

- Nagasawa, M. 1987, *Progress of Theoretical Physics*, 77, 635, doi: [10.1143/PTP.77.635](https://doi.org/10.1143/PTP.77.635)
- Ostriker, J. 1964, *ApJ*, 140, 1056, doi: [10.1086/148005](https://doi.org/10.1086/148005)
- Palmeirim, P., André, P., Kirk, J., et al. 2013, *A&A*, 550, A38, doi: [10.1051/0004-6361/201220500](https://doi.org/10.1051/0004-6361/201220500)
- Pedregosa, F., Varoquaux, G., Gramfort, A., et al. 2011, *Journal of Machine Learning Research*, 12, 2825
- Peretto, N., Fuller, G. A., André, P., et al. 2014, *A&A*, 561, A83, doi: [10.1051/0004-6361/201322172](https://doi.org/10.1051/0004-6361/201322172)
- Pezzuto, S., Benedettini, M., Di Francesco, J., et al. 2020, arXiv e-prints, arXiv:2010.00006. <https://arxiv.org/abs/2010.00006>
- Renaud, F. 2010, PhD thesis, -
- Rygl, K. L. J., Brunthaler, A., Sanna, A., et al. 2012, *A&A*, 539, A79, doi: [10.1051/0004-6361/201118211](https://doi.org/10.1051/0004-6361/201118211)
- Sault, R. J., Teuben, P. J., & Wright, M. C. H. 1995, in *Astronomical Society of the Pacific Conference Series*, Vol. 77, *Astronomical Data Analysis Software and Systems IV*, ed. R. A. Shaw, H. E. Payne, & J. J. E. Hayes, 433. <https://arxiv.org/abs/astro-ph/0612759>
- Schisano, E., Rygl, K. L. J., Molinari, S., et al. 2014, *ApJ*, 791, 27, doi: [10.1088/0004-637X/791/1/27](https://doi.org/10.1088/0004-637X/791/1/27)
- Schneider, N., Csengeri, T., Bontemps, S., et al. 2010, *A&A*, 520, A49, doi: [10.1051/0004-6361/201014481](https://doi.org/10.1051/0004-6361/201014481)
- Schneider, N., Csengeri, T., Hennemann, M., et al. 2012, *A&A*, 540, L11, doi: [10.1051/0004-6361/201118566](https://doi.org/10.1051/0004-6361/201118566)
- Schuller, F., André, P., Shimajiri, Y., et al. 2021, *A&A*, 651, A36, doi: [10.1051/0004-6361/202038259](https://doi.org/10.1051/0004-6361/202038259)
- Shimajiri, Y., André, P., Ntormousi, E., et al. 2019, *A&A*, 632, A83, doi: [10.1051/0004-6361/201935689](https://doi.org/10.1051/0004-6361/201935689)
- Tafalla, M., & Hacar, A. 2015, *A&A*, 574, A104, doi: [10.1051/0004-6361/201424576](https://doi.org/10.1051/0004-6361/201424576)
- Tigé, J., Motte, F., Russeil, D., et al. 2017, *A&A*, 602, A77, doi: [10.1051/0004-6361/201628989](https://doi.org/10.1051/0004-6361/201628989)
- Ward, J. H. 1963, *Journal of the American Statistical Association*, 58, 236, doi: [10.1086/160667](https://doi.org/10.1086/160667)
- Williams, G. M., Peretto, N., Avison, A., Duarte-Cabral, A., & Fuller, G. A. 2018, *A&A*, 613, A11, doi: [10.1051/0004-6361/201731587](https://doi.org/10.1051/0004-6361/201731587)
- Zapata, L. A., Loinard, L., Su, Y. N., et al. 2012, *ApJ*, 744, 86, doi: [10.1088/0004-637X/744/2/86](https://doi.org/10.1088/0004-637X/744/2/86)
- Zernickel, A., Schilke, P., & Smith, R. J. 2013, *A&A*, 554, L2, doi: [10.1051/0004-6361/201321425](https://doi.org/10.1051/0004-6361/201321425)

APPENDIX

A. ROBUSTNESS OF THE N_{H_2} AND T_{DUST} MAPS

In this section we discuss the uncertainties in the N_{H_2} map and the T_{dust} map (Figure 2) of the DR21(OH) ridge. The maps are derived through fitting the spectral energy distributions (SEDs) obtained from the continuum images in the three bands of *Herschel* 160 μm , JCMT 450 and 850 μm with a modified blackbody model (see Sect. 3.1). The flux uncertainty of each band used in the fitting is estimated as 20%. The 1- σ uncertainty maps of $\log_{10}N_{\text{H}_2}$ and T_{dust} derived in the SED fitting are shown in Figure A.1, which give an mean value of 0.11 dex and 1.6 K, respectively.

In the reduction of JCMT/SCUBA-2 data a largest angular scale is used to filter the independent low-frequency noise on the images (see Mairs et al. 2015). Its effect on the SED fitting can be seen as rises of temperature and temperature uncertainty on the map edges (Figures 2b and A.1b). For both our 450 and 850 μm data this scale is 480'' (3.5 pc@1.5 kpc), which is larger than our map sizes and thus has limited filtering effects in our region of interest (the three fibers in the middle of the maps).

The 850 μm continuum flux at DR21(OH) could potentially be contaminated by the strong free-free emission of this region. To evaluate this effect we adopt the radio SED relation of DR21(OH) in Araya et al. (2009) (see their Figure 5) and extrapolate it to 850 μm , which yields 66 mJy per 13''.7 beam. This is $\sim 1/400$ of the actual continuum intensity of DR21(OH) at 850 μm and can be neglected.

To examine the robustness of the 3-band SED fitting we derive another set of N_{H_2} and T_{dust} maps using the same techniques in deriving the 3-band ones but with continuum images in 6 bands of *Herschel* 160, 250, 350, 500 μm , and JCMT 450 & 850 μm . The resultant maps have a coarser resolution of 38''.5 and are presented in Figure A.2. The 3-band maps were then smoothed to this resolution and compared with the 6-band values as in Figure A.3. As indicated in the figure, 93% of the pixels in the temperature map have differences less than 2 K, and 90% of the pixels in the column density map have relative differences less than 25%. The N_{H_2} values derived with the 3-band data are on average 9% higher than the 6-band results, which is a result of the higher *Herschel* intensities at longer wavelengths compared with the JCMT ones (due to the large-scale filtering effect of the latter). The two fitting results agree with each other, with the overall uncertainties of fiber masses (see Appendix B).

B. UNCERTAINTIES OF THE FIBER MASSES

In this section we estimate the uncertainties of fiber masses. Figure B.1 presents the main sources of uncertainties in the derivation procedure of fiber masses, which can be divided into (1) uncertainties of assuming $T_{\text{ex}} = T_{\text{dust}}$ in fitting the H^{13}CO^+ spectra; (2) regional variations of the H^{13}CO^+ abundance; (3) SED fitting errors of the N_{H_2} as discussed in Sect. A; (4) distance uncertainty in parallax measurement. Here we discuss them respectively.

In the spectral fitting procedure we made the assumption of $T_{\text{ex}} = T_{\text{dust}}$ (Sect. 3.2). This assumption seems to be reasonable for the DR21(OH) ridge since the H_2 volume densities of its most parts exceed a few 10^4 cm^{-3} , which is sufficient for the dust and gas to be thermally coupled via collision (Hollenbach et al. 1991). At positions where the fibers are seen, the density is even higher. Here we implement the spectral fitting with varying T_{ex} to study its influence on the resultant tracer density $N_{\text{H}^{13}\text{CO}^+}$. We randomly select 1,000 out of the 7,625 H^{13}CO^+ spectra and for each spectrum we assign the fixed T_{ex} parameter with 50 random values respectively and do the spectral fitting repeatedly. The random temperature values observe a normal distribution with a mean equal to the dust temperature of that pixel and a standard deviation of 4 K. The resultant $N_{\text{H}^{13}\text{CO}^+}$ values obtained from the spectral fitting are compared with the original ones. As shown in Figure B.2, the uncertainties in T_{ex} introduce a 1- σ relative error of 12.1% in $N_{\text{H}^{13}\text{CO}^+}$ and N_{H_2} of the fibers.

When converting $N_{\text{H}^{13}\text{CO}^+}$ to N_{H_2} for the fibers a constant H^{13}CO^+ abundance is assumed (Sect. 3.4), which can be violated if the abundance has regional variations. To compare the two column densities we generated a $N_{\text{H}^{13}\text{CO}^+}$ map with the spectral fitting results, smoothed it to the resolution of the N_{H_2} map (Figure 2b), and re-gridded it to the same pixel frame. Figure B.3 plots the relation of N_{H_2} versus the abundance and the distribution of the abundance. There is no significant correlation between the two quantities, which indicates that $N_{\text{H}^{13}\text{CO}^+}$ is an overall good tracer of N_{H_2} and that adopting a constant abundance value is robust. The 1- σ regional variation of the H^{13}CO^+ abundance is 0.25 dex, which results in a relative uncertainty of 61% in N_{H_2} of the fibers.

To summarize, the uncertainty of T_{ex} , the regional variation of H^{13}CO^+ abundances, and the errors in SED fitting contribute independently to the relative uncertainty of fiber N_{H_2} by 12.1%, 61%, and 25.6%, respectively, which yield an overall uncertainty of 67.3%. For fiber masses, the uncertainty in distance measurements should be considered given $M \propto N_{\text{H}_2} D^2$. We adopt the

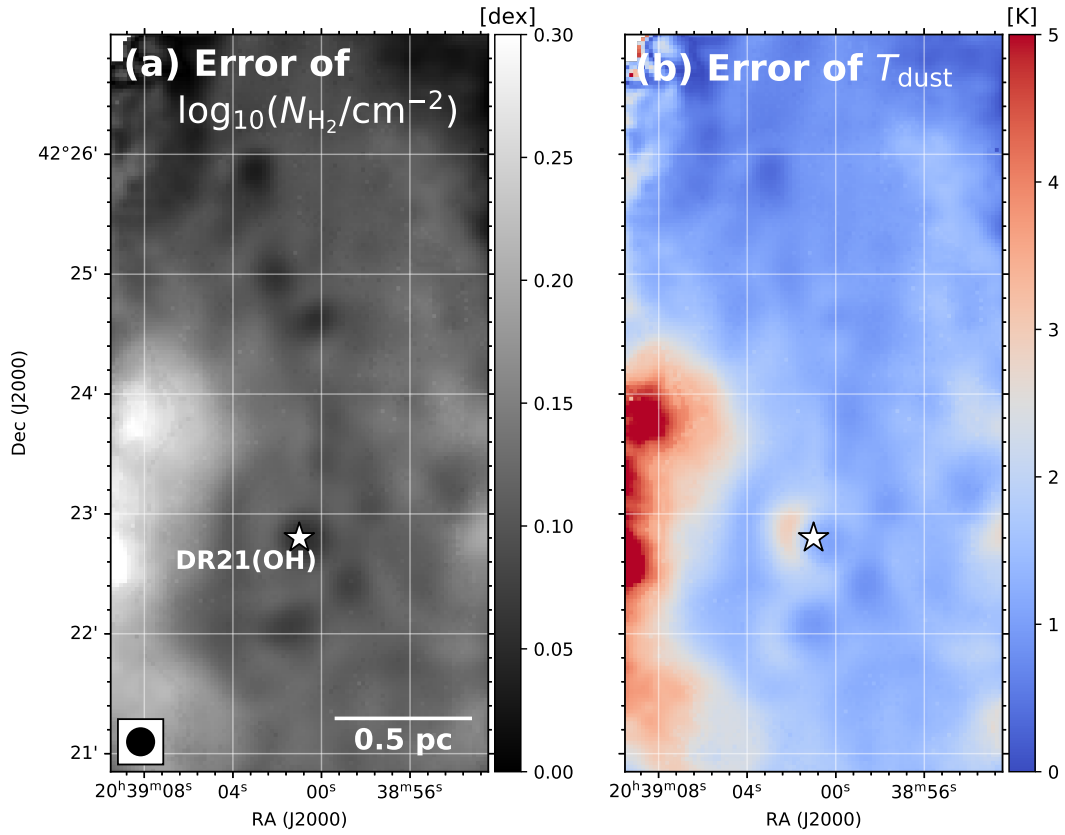


Figure A.1. Maps of the 1- σ uncertainties of (a) N_{H_2} and (b) T_{dust} derived from the SED fitting procedure (Sect. 3.1).

number of 5% in Rygl et al. (2012), which causes an uncertainty of 10% in mass. The overall uncertainty of fiber masses is then estimated to be 68%.

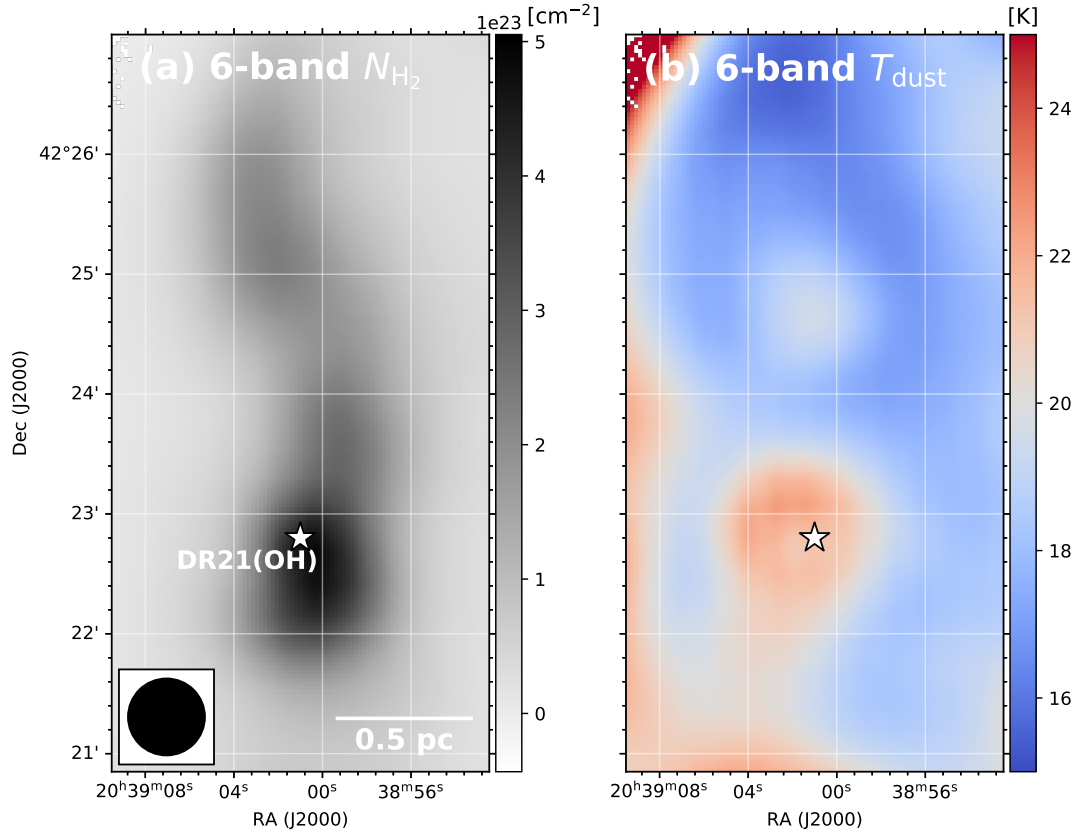


Figure A.2. Maps of (a) N_{H_2} and (b) T_{dust} derived with the 6-band continuum data (*Herschel* 160, 250, 350, and 500 μm ; JCMT 450 and 850 μm).

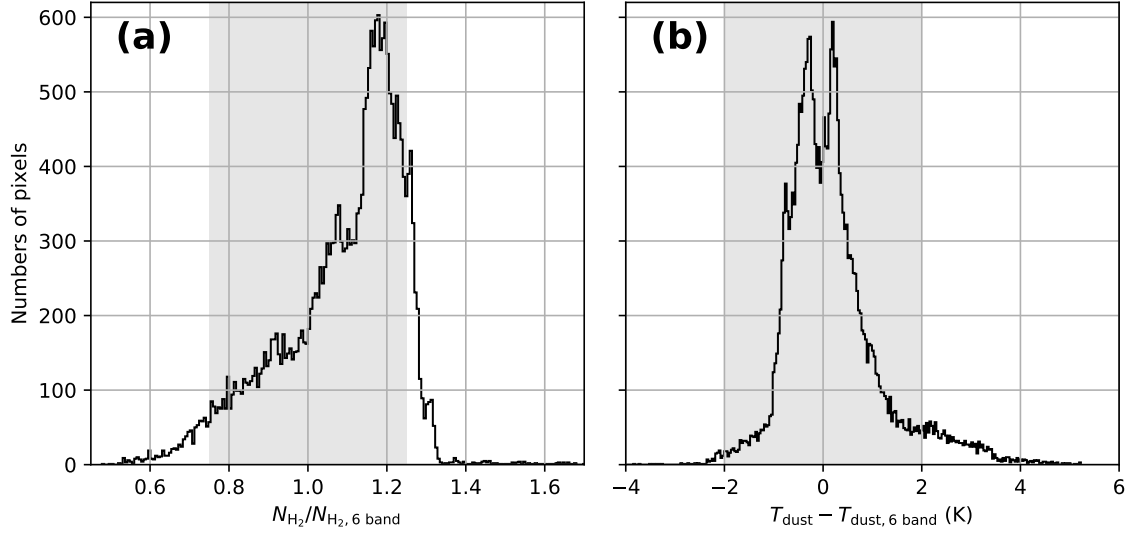


Figure A.3. Distributions of the differences in (a) N_{H_2} and (b) T_{dust} between the 3-band data and the 6-band data. The gray shaded regions show the pixels with (a) $|N_{\text{H}_2}/N_{\text{H}_2,6 \text{ band}}| \leq 25\%$ and (b) $|T_{\text{dust}} - T_{\text{dust},6 \text{ band}}| \leq 2 \text{ K}$, which take up 90% and 93% of the total number of pixels, respectively.

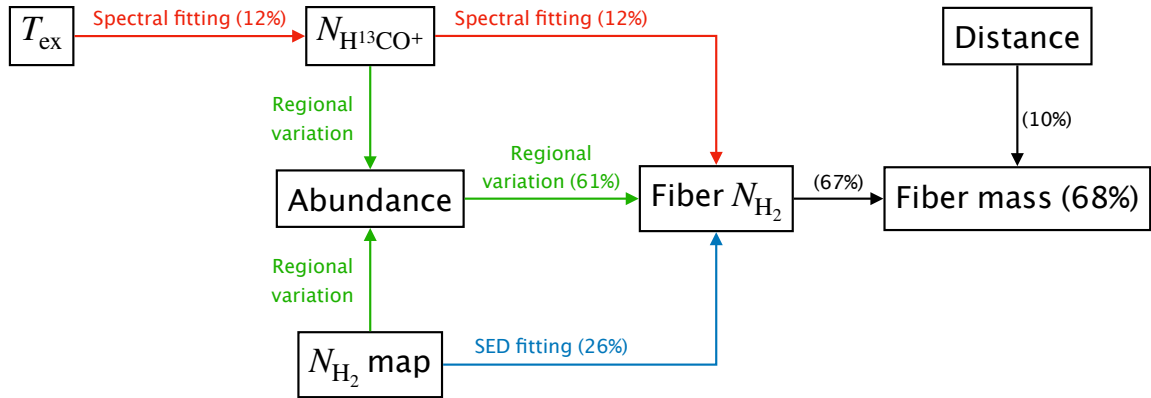


Figure B.1. Diagram showing the sources of errors in fiber masses and their transfer along the derivation procedure. The red, green, and blue connecting arrows represent the three major sources of errors in N_{H_2} of fibers discussed in Sect B. Percentages in brackets on the connecting arrows are the uncertainties of the *next* blocks contributed from the previous ones. The overall uncertainty of fiber masses is estimated to be 68%.

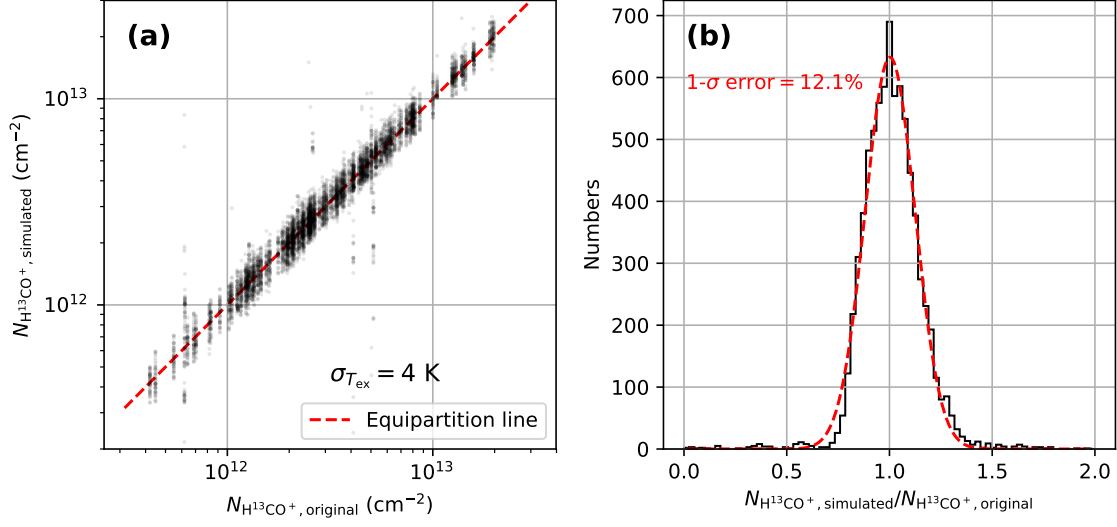


Figure B.2. (a) $H^{13}CO^+$ column densities derived from the original spectral fitting (Sect. 3.2) versus those derived with simulated excitation temperatures (Appendix B). (b) Distributions of the ratios of the two column densities. A Gaussian fitting is shown as the red dashed line.

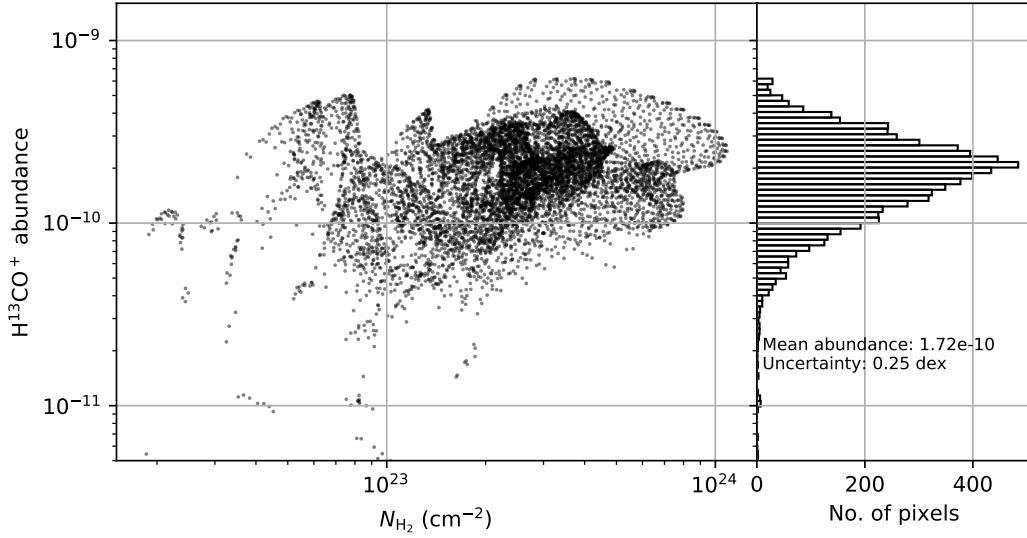


Figure B.3. H_2 column density versus the abundance of $H^{13}CO^+$ of each pixel of the H_2 column density map (Figure 2b). Histogram of the $H^{13}CO^+$ abundance is also shown on the right.